

**Moderate Resolution Imaging Spectroradiometer (MODIS)  
Downward Shortwave Radiation (MCD18A1) and  
Photosynthetically Active Radiation (MCD18A2)  
Algorithm Theoretical Basis Document**

Collection 6

Shunlin Liang, Dongdong Wang

Department of Geographical Sciences  
University of Maryland, College Park

September 2017

## Change History Log

<b>Version</b>	<b>Description of changes</b>	<b>Prepared by</b>	<b>Date</b>
1.0	New ATBD document developed for NASA review	Shunlin Liang	Nov 2010
2.0	Changing details on PAR and DSR algorithms according to the operational implementation, adding sections on sensitivity analysis, product generation and description, updating validation results	Dongdong Wang Shunlin Liang	Aug 2017

## Table of Contents

Abstract .....	4
1. Introduction.....	5
2. Algorithm descriptions.....	7
2.1 Background .....	7
2.2 MODTRAN simulations .....	8
2.3 Creating and searching LUTs.....	9
2.4 Water vapor correction.....	11
2.5 Sensitivity study .....	11
2.6 Product generation.....	15
2.7 Product description.....	17
3. Validation.....	17
3.1 Algorithm validation .....	17
3.2 Product validation .....	20
4. Constraints, limitations, and assumptions.....	21
5. References .....	21

## Abstract

Incident solar radiation is the major source of energy over land surfaces. It controls the exchange of matter and energy between the land surface and the atmosphere. Downward shortwave radiation (DSR) and its visible portion, photosynthetically active radiation (PAR) over land surfaces, are required by almost all land surface models. Previous satellite products of DSR and PAR typically have coarse spatial resolution that cannot meet the requirements of land process modeling and data analysis.

Funded through the NASA ROSES 2013 program, operational global high-resolution (5km) land DSR (MCD18A1) and PAR (MCD18A2) products were recently developed from MODIS data. The retrieval is based on an efficient look-up-table approach that can work at the native resolution of MODIS data. The original algorithm was developed by Liang et al. (2006) for estimating PAR from MODIS data. After a decade of algorithm refinements and improvements, the current algorithm has become mature and robust.

The algorithm has been validated extensively in various previous studies. Although it is intended for generating high-resolution (~km) products, the validation results have shown accuracy generally better than that of the existing coarse-resolution products. Recent validation of the actual MCD18A1 and MD18A2 products using ground measurements suggests that the new high-resolution MODIS land surface radiation products are reliable and highly accurate. DSR and PAR have the overall coefficients of determination of 0.91 and 0.92 respectively. MCD18A1 has a root mean square error (RMSE) of  $90 \text{ W/m}^2$ , bias of  $17 \text{ W/m}^2$ . MCD18A2 has a RMSE of  $39 \text{ W/m}^2$ , bias of  $9 \text{ W/m}^2$ .

This Algorithm Theoretical Basis Document (ATBD) provides a summary of the theoretical description and the physical basis for the algorithms of generating MCD18A1 and MCD18A2 products, as well as the evaluation of the algorithms and the products.

# 1. Introduction

Solar radiation is the major source of energy over land surfaces and controls the exchange of matter and energy between the Earth's surface and its atmosphere. Incident solar radiation over land surface is a key variable in the study of a variety of scientific and application issues related to climate changes, hydrologic, bio-physical and bio-chemical modeling, solar energy applications, and agriculture (Liang et al. 2010).

Altering surface shortwave radiation forcing will lead to significant adjustments in surface temperature, moisture and fluxes during the resulting complex land surface thermodynamic and hydrological processes. This, in turn, will affect the surface heat and moisture budget as well as biological productivity (Wild 2012). As the driving force, downward shortwave radiation (DSR) and its visible portion, photosynthetically active radiation (PAR) over land surfaces are required by almost all land surface models.

Radiation, temperature, and water interact to impose complex and varying limitations on vegetation activity in different parts of the world. Nemani et al. (2003) estimated that radiation limits vegetation growth over 27% of Earth's vegetated surface. Almost all ecosystem models contain the physiological processes involved in photosynthesis and stomatal regulation that control the exchange of water vapor and carbon dioxide ( $CO_2$ ) between vegetation canopies and the atmosphere. Gross primary productivity (GPP) of vegetation canopy is often calculated using the production efficiency models:

$$GPP = \varepsilon \times FAPAR \times PAR, \quad (1)$$

where  $\varepsilon$  is the radiation efficiency factor defined by different models,  $FAPAR$  represents the fraction of PAR absorbed by the green vegetation which has been a satellite product from many sensors (Baret et al. 2007; Myneni et al. 2002; Xiao et al. 2015), but PAR is not. Cramer et al. (1999) made a model intercomparison and found that many widely used models utilize the production efficiency principles, such as CASA (Potter et al. 1993), SiB (Sellers et al. 1986) and GLO-PEM (Prince and Goward 1995). MODIS PSN/NPP product algorithm (MOD17) is also based on this formulation (Zhao et al. 2006). All these models require PAR data. Cai et al. (2014) recently demonstrated that high-resolution accurate PAR inputs can significantly improve the GPP calculation.

Terrestrial evapotranspiration (ET) on average uses approximately 59% of the surface net energy (Trenberth et al. 2009), which is largely determined by surface DSR. In fact, many satellite ET algorithms, including the MODIS ET (MOD16), directly depend on DSR (Wang and Dickinson 2012). To initiate, calibrate, diagnose, and validate these algorithms and models, accurate inputs of DSR are imperative.

Extraterrestrial downward shortwave radiation (at top-of-atmosphere (TOA)) is mainly governed by solar zenith angle (SZA) and the distance between the Sun and the Earth. In addition to SZA and the Sun-Earth distance, DSR or PAR that reaches the land surface is largely determined by absorption and scattering of the atmospheric constituents. Additionally, multiple scattering between the atmosphere and the surface also contributes to their variability. Given the high dynamics and spatial variations of these two parameters, satellite remote sensing is the only practical and effective way to map global DSR and PAR.

The World Meteorological Organization (WMO) specified requirements of DSR products for three types of applications (See Table 1), but no existing radiation products can meet these requirements. The current global radiation datasets derived mostly from satellite observations have much coarser spatial resolutions, such as Clouds and the Earth's Radiant Energy System (CERES) product (Wielicki et al. 1998) at a spatial resolution of 140km from 1997 to present, the International Satellite Cloud Climatology Project (ISCCP) product on a 280 km equal-area global grid from 1983-2008 (Zhang et al. 2004), the Global Energy and Water Cycle Experiment (GEWEX) surface radiation budget (SRB) product at a spatial resolution of 1° x 1° from 1983-2007 (Pinker et al. 2003).

**Table 1.** WMO observation requirements for surface downward shortwave radiation. NWP: Numerical Weather Prediction, AOPC: Atmospheric Observation Panel for Climate. (<https://www.wmo-sat.info/oscar/variables/view/50>, last visited on August 9, 2017)

Applications	Uncertainty goal ( $\text{Wm}^{-2}$ )	Uncertainty threshold ( $\text{Wm}^{-2}$ )	Horizontal resolution goal (km)	Horizontal resolution threshold (km)
Global NWP	1	20	10	100
Agricultural Meteorology	N/A	N/A	1	20
Climate-AOPC	5	10	25	100

Another issue is that current insolation products do not have the accuracy required for land surface applications (Liang et al. 2010). Hicke (2005) found that global mean National Center for Environment Prediction (NCEP) solar radiation exceeded that from ISCCP by 16%, and locally, relative differences were up to 40% in the mean and 10% in the trend of solar radiation and varied in sign across the globe. Gui et al. (2010) compared three satellite-based surface insolation datasets (GEWEX-SRB, ISCCP-FD, and CERES-FSW) and demonstrated large biases in Southeast Asia, the Tibet Plateau, and Greenland. For example, the  $R^2$  value of the validation results in the Tibet Plateau for CERES-FSW data is only 0.35. In a more recent study assessing existing satellite DSR products, Zhang et al. (2015) found that satellite products agree better with surface measurements at monthly than at daily time scale but all four satellite products analyzed overestimate DSR by approximately  $10 \text{ W m}^{-2}$ .

Methods to estimate incident shortwave radiation fluxes from satellite data can be roughly divided into two categories according to whether products of atmospheric and surface parameters or data of top-of-atmosphere (TOA) radiance are the major source of information.

DSR and PAR can be accurately calculated by radiative transfer models (RTM) under the approximation of plane parallel atmosphere if surface BRDF and vertical profile of atmosphere constituents such as gas molecules, aerosols and clouds are known. This constitutes the basis of the first type of methods. These methods can be further divided into (a) directly running RTMs and (b) using parameterization. To improve computational efficiency of running RTMs, the simple two-stream approximations for multiple scattering or even simpler schemes are typically used. Computation is speeded up significantly with the simplified models, but they usually are inaccurate in calculating multiple scattering that dominates when the atmospheric optical depth is large (hazy or cloudy) and/or the surface is very bright (snow/ice). An alternative approach is by parameterizing to simplify radiative transfer processes and obtain approximation of DSR and PAR (Qin et al. 2015; Tang et al. 2016).

The second types of methods directly estimate DSR or PAR from TOA radiance data, which can avoid error propagation resulted from uncertainties in input atmospheric parameters. For example, Liang et al. (2006) developed a look-up-table (LUT) based method algorithm to estimate incident PAR over land surfaces from time series data of MODIS TOA radiance. It is specifically designed to achieve the high accuracy and keep a simple form of the model. This algorithm was then extended to estimate PAR from AVHRR data (Liang et al. 2007). Liu et al. (2008) revised this method by using MODIS surface reflectance product (MOD09). Wang et al. (2010) presented a new algorithm for integrating instantaneous PAR values from MODIS data to produce a daily PAR product. Zheng et al. (2008) extended the MODIS PAR algorithm to GOES data. Lu et al. (2010) adapted the MODIS algorithm to another geostationary satellite GMS5 data to map incident PAR in China. Zhang et al. (2014) further improved this algorithm suitable for global production. Through these algorithm refinements and improvements, this approach is becoming mature and robust.

Funded through the NASA ROSES 2013 program, we optimized the research and prototype codes and operationally implemented this LUT-based algorithm. The global high-resolution land DSR (MCD18A1) and PAR (MCD18A2) products are being generated from the MODIS data. Such high resolution products of DSR and PAR are essential for serving as upstream input for MODIS NPP and ET products, driving high resolution land surface models and investigating scientific questions of surface radiation at local or regional scales. Cai et al. (2014) recently demonstrated that high-resolution accurate PAR inputs can significantly improve the GPP calculation. The high resolution products also play an vital role in validating coarse resolution data sets, such as reanalysis products (Zhang et al. 2016).

This Algorithm Theoretical Basis Document (ATBD) provides a summary of the theoretical description and the physical basis for the algorithms of generating MCD18A1 and MCD18A2 products, as well as the evaluation of the algorithms and the products.

## **2. Algorithm descriptions**

The basic framework of the algorithms was presented by Liang et al. (2006). It was for estimating incident PAR from MODIS data. The algorithm first estimates surface reflectance from multi-temporal imagery and then appraises PAR flux for each imagery. The basic procedure consists of two steps: (1) determination of the surface reflectance from observations under the “clearest” atmospheric conditions in a temporal window or reprocessed from the MODIS surface reflectance product; and (2) calculation of incident PAR from the determined surface reflectance and TOA radiance/reflectance by searching the LUTs. The LUTs are pre-calculated from comprehensive simulations of atmospheric radiative transfer models, storing radiative transfer parameters as a function of atmospheric visibility index (aerosol or cloud optical depth) at different viewing geometries. Theoretical background and practical consideration on this algorithm are described in details as follows.

### **2.1 Background**

Satellite TOA observations contain information from both the atmosphere and the land surface. Under the assumption of Lambertian surfaces, TOA spectral radiance recorded by a satellite radiometer can be approximated by the following formula (Liang 2004):

$$I(\mu_0, \mu, \phi) = I_0(\mu_0, \mu, \phi) + \frac{r_s}{1 - r_s \bar{\rho}} \mu_0 E_0 \gamma(-\mu_0) \gamma(\mu) \quad , \quad (2)$$

where  $I(\mu_0, \mu, \phi)$  is TOA spectral radiance for a given viewing geometry (solar zenith angle  $\theta_0$  ( $\mu_0 = \cos(\theta_0)$ ), view zenith angle  $\theta$  ( $\mu = \cos(\theta)$ ), and relative azimuth angle  $\phi$ ). The first part of the left side  $I_0(\mu_0, \mu, \phi)$  represents path radiance and the second part contains the contribution from the surface and the atmosphere as well as the multiple scattering between the surface and the atmosphere.  $r_s$  is surface reflectance,  $E_0$  is the extraterrestrial solar irradiance,  $\gamma(\mu_0)$  is the total transmittance (direct plus diffuse) in the solar illumination direction,  $\gamma(\mu)$  is the total transmittance (direct plus diffuse) in the sensor viewing direction.

Similarly, incident solar radiation can also be formulated as a function of atmospheric and surface parameters. Surface incident solar radiation depends mainly on atmospheric properties, but also to a lesser extent on surface reflectance. It can be demonstrated by the following formula for calculating downward spectral flux  $F(\mu_0)$  at the solar zenith angle  $\theta_0$  over a Lambertian surface (Liang 2004):

$$F(\mu_0) = F_0(\mu_0) + \frac{r_s \bar{\rho}}{1 - r_s \bar{\rho}} \cdot E_0 \cdot \mu_0 \cdot \gamma(\mu_0) \quad , \quad (3)$$

where  $F_0(\mu_0)$  is the downward flux without any contributions from the surface, the definition of other parameters is the same as that of Eq (2). It is clear that the surface contribution to the incident flux mainly depends on  $r_s \bar{\rho}$ . If the atmosphere is very clear (i.e.,  $\bar{\rho}$  is small) or the surface reflectance  $r_s$  is low, the surface contribution to the incident flux is relatively small.

All radiometric variables are functions of wavelength. Integration of the downward spectral fluxes from Eq(3) will produce broadband fluxes, such as DSR and PAR. PAR use the spectral range of 400 nm to 700 nm and DSR uses 300 and 2500nm:

$$PAR(\mu_0) = \int_{400}^{700} F_\lambda(\mu_0) d\lambda \quad , \quad (4a)$$

$$DSR(\mu_0) = \int_{300}^{2500} F_\lambda(\mu_0) d\lambda \quad . \quad (4b)$$

## 2.2 MODTRAN simulations

Instead of online calculation of various atmospheric functions in Eq 2-4 on the pixel basis that can be computationally very expensive, they are tabled (as LUT) offline as a function of atmospheric visibility index (aerosol or cloud optical depth) at different viewing geometries.



Two LUTs are created through radiative-transfer simulation by MODTRAN. The first table is used to compare the actual with simulated TOA reflectance to derive atmospheric conditions; the second table is used to estimate instantaneous surface radiative fluxes using atmospheric conditions derived from the first look-up table. Detailed information on the parameters used to create the two LUTs during radiative-transfer simulation is summarized in Table 2.

**Table 2.** Summary of key parameters used in running MODTRAN simulations for generating a look-up table (LUT). For each combination of these parameters, three surface reflectance values are specified in MODTRAN. MODTRAN outputs at each wavelength interval for these three surface reflectance are used to solve for the parameters used in Eq(2) and Eq(3).

<b>Input parameters</b>	<b>Values</b>
Solar zenith angle	0°, 15°, 30°, 45°, 55°, 65°, 75, 85°, 90°
View zenith angle	0°, 20°, 40°, 60°, 80°
Relative azimuth angle	0°, 30°, 60°, 90°, 120°, 150°, 180°
Surface altitude	0.0, 1.0, 2.0, 3.0, 4.0, 5.0 (km)
Aerosol type	Rural aerosol
Cloud type	Altostratus cloud
Aerosol loadings (visibility)	5, 10, 20, 30, 100 (km)
Cloud extinction coefficient	92.0, 60.0, 40.0, 20.0, 10.0, 5.0, 3.0, 2.0, 1.0, 0.5, 0.2, 0.05 (km <sup>-1</sup> )
Water vapor amount	Default value
Ozone amount	Default value

For each value of visibility index at each specific sun-viewing geometry, three surface reflectance values are specified (0.0, 0.5 and 0.8) for the range of wavelengths in MODTRAN. MODTRAN outputs at each wavelength interval for these three surface reflectance are used to solve for the parameters used in Eq(2) and Eq(3). These quantities are then integrated with the MODIS sensor spectral response functions over wavelength to get the average values for each wave band.

### 2.3 Creating and searching LUTs

Once the two LUTs have been generated through radiative transfer simulation, DSR and PAR can be derived. The workflow for searching the look-up tables is as follows. First, TOA reflectance or radiance is calculated using the digital numbers (DNs) for the corresponding bands from actual satellite observational data. Then surface reflectance data are derived from MODIS land-surface reflectance data (MOD09A1). Next, TOA radiance is calculated for each atmospheric condition, ranging from the clearest conditions (high surface meteorological range) to the cloudiest conditions (high cloud extinction coefficient) under various geometries using the LUT generated at the satellite level. Then the actual TOA radiance derived from the selected sensor bands is compared with the calculated radiances under all atmospheric conditions and various geometries using the TOA LUT to retrieve the atmospheric index, which is defined as the index of the atmospheric conditions in the study. Finally, DSR and PAR can be obtained

using the retrieved atmospheric index and the derived surface reflectance under various geometries using the LUT at the surface level.

In the initial algorithm, the approach of “clearest” observations was used to estimate surface reflectance for each pixel. This approach needs stack of time series data and also suffers from the issues of surface changes and cloud shadow. Satellite products of surface reflectance were used in a follow-up study (Liu et al. 2008) and proved to be able to generate robust results. Here, the MODIS land surface reflectance product (MOD09A1) is used in the current algorithm.

A temporal filter was applied to the MOD09A1 time series to reduce the effects of residual clouds on surface reflectance and fill data gaps caused by persistent cloud coverage (Tang et al. 2013). The core of this temporal filter algorithm is a time series cloud detection (TSCD) algorithm. It is based on the relative stability of ground reflectance and the sudden variations in reflectance that result from cloud cover.

The algorithm first searches the clear-sky reference data, and then discriminates clouded and unclouded pixels by detecting a sudden change of reflectance in the blue wavelength and spectral correlation coefficient at the pixel level. For each date  $D$ , the clear reference pixel contains the most recent cloud-free reflectance obtained in the time series before date  $D$ . A pixel is labeled as clear for the time series criterion if

$$\left| \rho_{b_3}(D) - \rho_{b_3}(D_r) \right| < K_1(D - D_r) + L_1, \quad (5)$$

$$\text{corr}(D, D_r) = \cos(\theta_{D, D_r}) > L_2 - K_2(D - D_r) \approx 0.96, \quad (6)$$

where  $\rho_{b_3}(D)$  is the surface reflectance of the pixel in the blue band at date  $D$ ,  $D_r$  is the date of the most recent clear data before, and  $\text{corr}(D, D_r)$  is the normalized spectral correlation coefficient, where  $\theta_{D, D_r}$  is the spectral angle between  $\rho(D)$  and  $\rho(D_r)$ .  $K_1$ ,  $L_1$ ,  $K_2$ , and  $L_2$  are coefficients whose threshold values depend on  $D - D_r$ .  $K_1$  and  $K_2$ , which characterize the change of the spectra and correlation coefficient with time, are related to the land type and season alteration.  $L_1$  and  $L_2$  represent the effects of BRDF and noise.

Two kinds of clear sky cases need to be determined: the first clear sky in the time series, and all subsequent clear skies. Once the first clear sky is determined, the subsequent clear sky is easier to obtain. In order to save computing time, a subsequent pixel will be labeled as clear if Eq (5) and (6) are satisfied. Then, the reference clear sky will be substituted with the new clear sky. Searching for subsequent clear sky will continue until a new clear sky could not be found for more than 80 days. At this time, the object may have changed suddenly because of land cover change or because of cropping, for instance, so the idea is to restart the search for a new first clear sky since the last clear sky.

## 2.4 Water vapor correction

Water vapor absorbs infrared radiation and the influence of water vapor on the estimation of the surface radiation is significant, especially in the infrared band under cloud-free conditions. The water vapor broadband and spectral transmission parameterization functions have been reported in the literature. During the radiative transfer simulations through MODTRAN, the default amount of water vapor was utilized.

To reduce the water vapor influences on DSR estimation, a simple normalized water vapor transmittance method was used for the water vapor correction of the solar radiation at the surface. The correction method is applied only to the DSR estimation (not the PAR estimation) because water vapor absorption primarily occurs in the infrared spectrum.

The water vapor transmission rate index  $T_w$  can be estimated using the following equation (Psiloglou et al. 2000):

$$T_w = 1 - \frac{3.014 Mu}{(1 + 119 .3 Mu )^{0.644} + 5.814 Mu}, \quad (7)$$

where  $M$  is the optical atmospheric mass, and  $u$  is the water vapor amount in cm. The optical air mass  $M$  can be obtained as according to the following equation:

$$M = (\cos \theta_s + 0.50572 (96 .07995 - \theta_s)^{-1.6364})^{-1}, \quad (8)$$

where  $\theta_s$  is the solar zenith angle. After the water vapor transmittance is calculated, it is normalized by the following equation:

$$R_w = T_w(u) / T_w(u_d), \quad (9)$$

where  $R_w$  is the normalized water vapor transmittance,  $T_w(u)$  is the water vapor transmittance at the water vapor amount  $u$  in cm, and  $T_w(u_d)$  is the water vapor transmittance at the default amount of water vapor. The estimated DSR at the surface is then corrected using the normalized water vapor transmittance  $R_w$ .

## 2.5 Sensitivity study

To better evaluate the interactions of these atmospheric input variables in the LUT, a sensitivity analysis of the atmosphere profiles, ozone level, water vapor amount, surface elevation, and aerosol model was performed.

The six standard atmosphere profiles (tropical, midlatitude winter, midlatitude summer, sub-Arctic winter, sub-Arctic summer, and 1976 US standard) were employed with specified atmosphere variables. The influences of the atmosphere profiles on the estimation of DSR and

PAR are illustrated in Figure 1. The standard deviation (STD) of the simulated DSR and PAR values with selected atmosphere profiles is  $22 \text{ Wm}^{-2}$  and  $2.2 \text{ Wm}^{-2}$ , respectively. The large STD of the DSR is caused by the Arctic winter profiles; the STD is reduced to  $7 \text{ Wm}^{-2}$  when these atmosphere profiles are excluded. Thus, we can conclude that the DSR and PAR simulations are not sensitive to the atmosphere profiles for this algorithm.

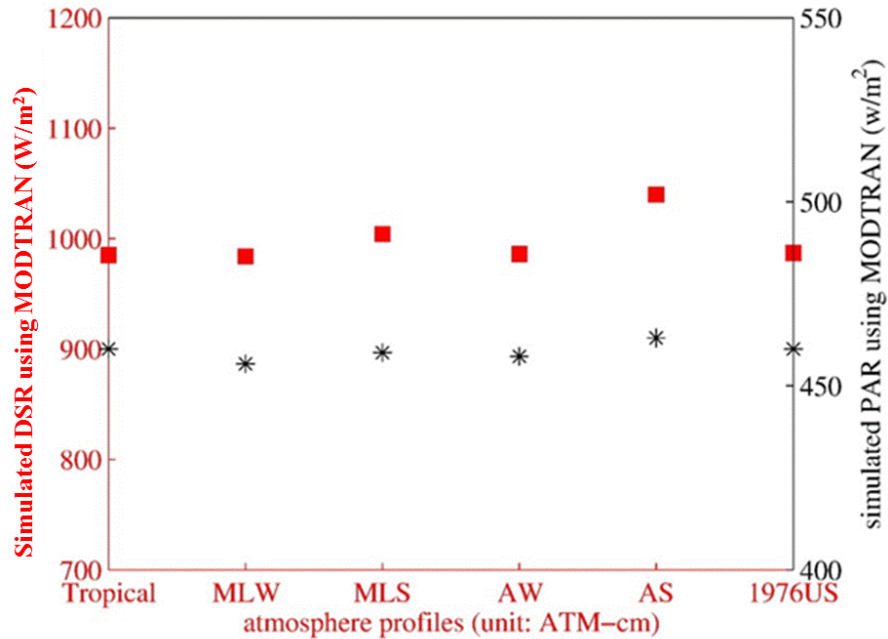


**Figure 1.** Sensitivity of PAR and DSR estimates to atmosphere profiles. The atmospheric condition is represented by a mid-latitude winter atmosphere with a rural aerosol type. Other input atmospheric variables are set as constants (solar zenith angle,  $0^\circ$ ; visibility, 90 km; surface albedo, 0.2; cloud extinction coefficient,  $1 \text{ km}^{-1}$ ). MLW, MLS, AW, AS, and 1976US represent the mid-latitude winter, mid-latitude summer, Arctic winter, Arctic summer, and 1976 US standard atmosphere profiles, respectively.

The sensitivity experiments used to determine the dependence of DSR and PAR on the absorption of water vapor and ozone are shown in Figure 2 at mid-latitude summer atmospheric profiles using a rural aerosol model under cloud-free conditions and a visibility of 90 km, which is considered a very clear atmospheric condition. The other atmospheric parameters are set as constants in MODTRAN. As shown in Figure 2, the DSR and PAR estimates vary by approximately  $30 \text{ Wm}^{-2}$  and  $20 \text{ Wm}^{-2}$ , respectively, at the surface with the increasing ozone from 0.0 to 0.8 atm-cm. However, the amount of ozone does not change significantly under most conditions. Under other relatively hazy/cloudy air conditions, the influence of the ozone level is smaller. Thus, ozone is set as a constant in the simulation, and the effects of ozone are not corrected in our algorithm. The effects of water vapor on the estimation of DSR and PAR are also shown in Figure 2. Water vapor has a significant effect on DSR but is insignificant in terms

of the PAR calculation because the absorption of water vapor occurs primarily in the infrared band (Liu et al., 2008). Therefore, a simple water vapor correction function is applied to the DSR product.

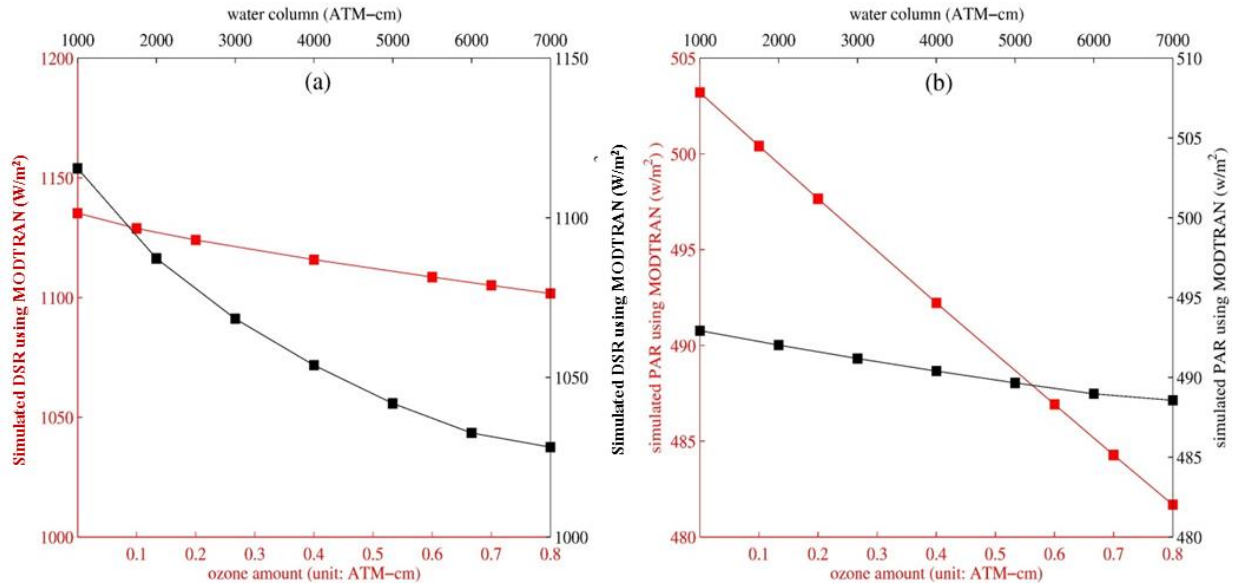


**Figure 2.** Sensitivity of (a) DSR and (b) PAR to variations in the amounts of ozone and water vapor. The atmospheric condition is represented by a mid-latitude summer atmosphere with a rural aerosol type. Other input atmospheric variables are set as constants (water vapor amount,  $2.0 \text{ gm}^2$ ; visibility, 90 km; albedo, 0.20).

The effects of surface elevation on DSR and PAR are also important and cannot be ignored, and there are many published reports on this topic (Dubayah 1992). Surface elevation effects are a dimension considered in the look-up table in our algorithm. The variations in the DSR and PAR estimates with changes in the surface elevation are described in Figure 3. We conclude that the influences of surface altitudes on DSR and PAR are significant under both cloudy conditions and cloud-free conditions and cannot be neglected. The surface elevation may cause an error of up to  $100 \text{ Wm}^{-2}$  and is a significant source of error in DSR and PAR estimation. For example, this effect is the most likely reason that a number of current radiation products have large errors over the Tibetan Plateau.

To evaluate the effects of aerosol models on DSR and PAR simulations using MODTRAN, we select four basic aerosol modes to represent atmospheric turbidity in MODTRAN. The sensitivities of DSR and PAR to selected aerosol modes (rural, maritime, urban, and tropospheric) under cloud-free conditions with 23 km of visibility are shown in Figure 4; this comparison shows that DSR and PAR have similar sensitivities to the various aerosol modes. In addition, the rural, maritime, and tropospheric aerosol modes do not have a significant influence on DSR and PAR, whereas the urban aerosol mode does have an effect. The maritime and urban aerosol modes affect the largest difference, reaching approximately 60 and  $29 \text{ Wm}^{-2}$  for DSR and PAR,

respectively, due to the strong absorption of solar radiation by urban aerosols. These results are consistent with the findings of Lu et al. (2010). The retrieval of DSR and PAR is affected by the distinct characteristics and size distributions of different aerosol modes under cloud-free conditions, especially in highly polluted regions (Wang et al., 2010). However, the influences of the aerosol modes on the estimation of solar radiation at the surface are not implemented in this algorithm because the aerosol influences are insignificant under cloudy conditions and significant under clear-sky conditions.

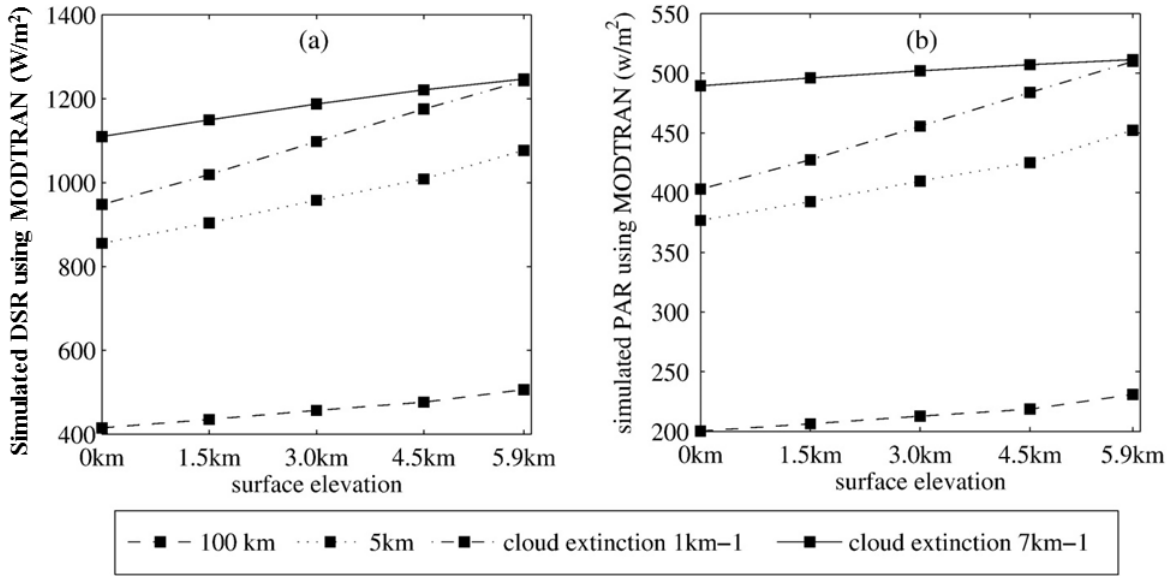


**Figure 3.** Sensitivity of (a) DSR and (b) PAR at the surface to the surface altitude under different atmosphere conditions (100 km visibility, 5 km visibility,  $1 \text{ km}^{-1}$  cloud extinction, and  $7 \text{ km}^{-1}$  cloud extinction of mid-latitude summer atmosphere with a rural aerosol type).

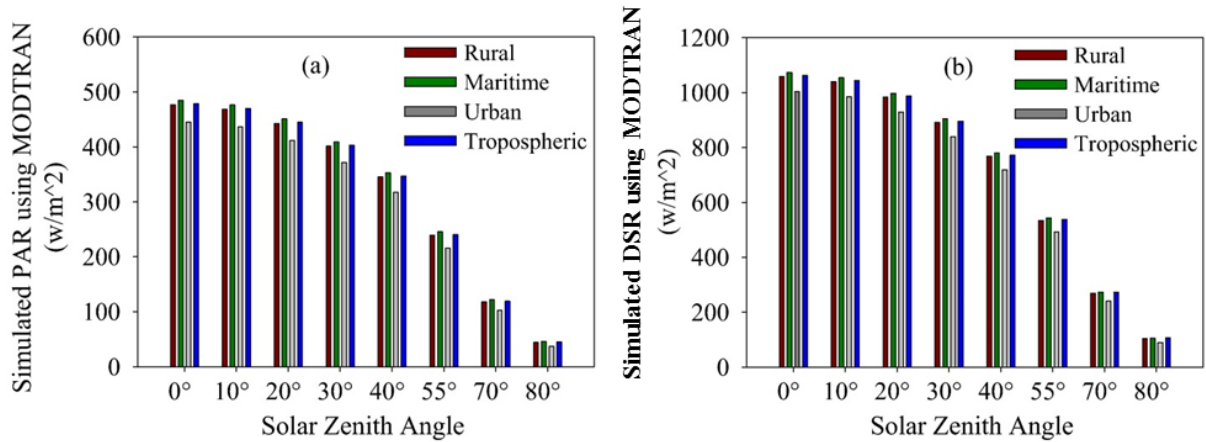


**Figure 4.** Sensitivity of (a) PAR and (b) DSR to aerosol modes under different solar zenith angles. The atmospheric condition is represented by a mid-latitude summer atmosphere. Other input atmospheric variables are set as constants (water vapor,  $2.0 \text{ gm/m}^2$ ; visibility, 23 km; albedo, 0.20).

Similarly, six cloud types (including cumulus, altostratus, stratus, stratocumulus, nimbostratus, and cirrus) were chosen in order to evaluate their effects on DSR and PAR simulations using MODTRAN. The sensitivities of DSR and PAR to cloud types are shown in Figure 5; this comparison shows that DSR and PAR have similar sensitivities to the various cloud types. The clouds of cumulus, stratus, stratocumulus, nimbostratus, and cirrus generate similar values of DSR and PAR, whereas the altostratus cloud results in slightly smaller values of DSR and PAR. Even for altostratus, the difference is only about 30 W/m<sup>2</sup>. The simulation suggests that the cloud types do not lead to significant uncertainty in estimating incident shortwave radiative fluxes. These results are consistent with the findings of Liang et al. (2006) on PAR and Kim and Liang (2010) on net shortwave radiation. Thus, the influences of the cloud types on the estimation of solar radiation at the surface are not implemented in this algorithm and a single cloud type was used in establishing LUTs.

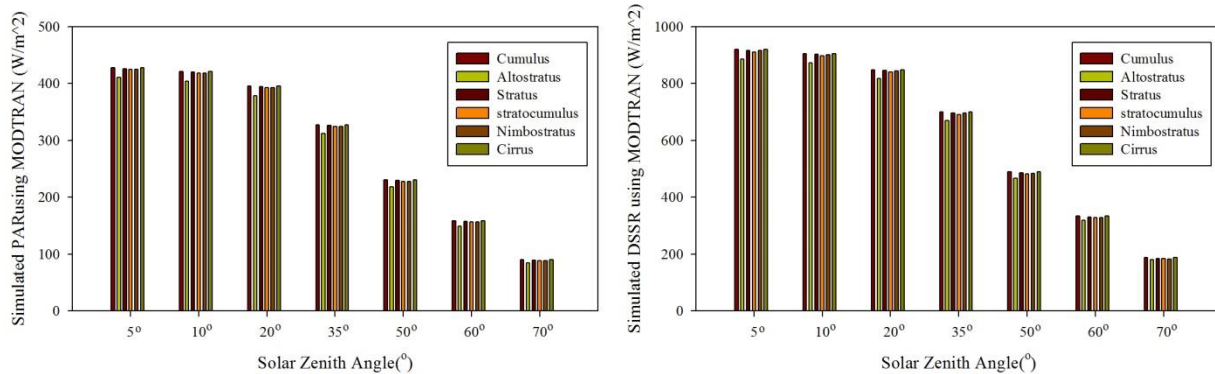


**Figure 5.** Sensitivity of (a) PAR and (b) DSR to cloud types under different solar zenith angles. Other input atmospheric variables are set as constants (cloud optical depth, 1.5; water vapor, 3.0 gm/m<sup>2</sup>; albedo, 0.10).

## 2.6 Product generation

Data production will use both MODIS Terra and Aqua data. MCD18A1 and MCD18A2 are gridded L3 products in MODIS sinusoidal map projection. The instantaneous values of DSR and PAR corresponding to MODIS overpass time can be directly estimated using the abovementioned LUT approach. These instantaneous results are saved as one data layer of MCD18A1 and MCD18A2 files.

To better meet users' requirements, values of DSR and PAR are also retrieved every 3 hour at GMT 0:00, 3:00, 6:00, 9:00, 12:00, 15:00, 18:00, and 21:00. The DSR and PAR at the 3-hour intervals are estimated using the visibility index of the closest MODIS overpass time. This interpolation method assumes that the atmospheric condition varies only slightly during a given period. With the visibility index, DSR and PAR can be estimated using Eq (2). To obtain parameters of Eq (2) from the LUTs, the value of solar zenith angle is also needed.

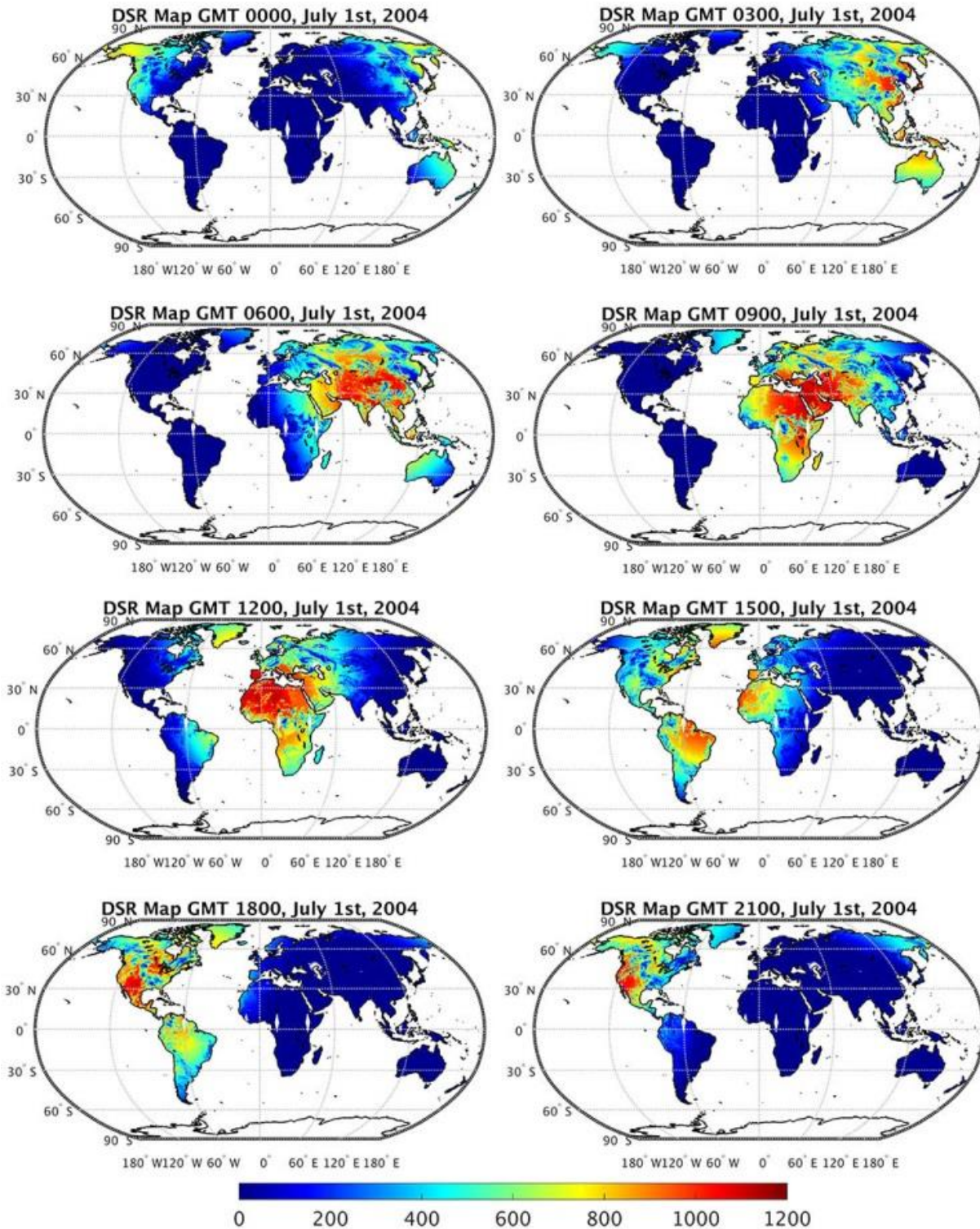


**Figure 6.** Global maps of 3-hourly DSR on July 1 2004. The eight 3-hour maps are for GMT 0:00, 3:00, 6:00, 9:00, 12:00, 15:00, 18:00, and 21:00 respectively. Data over the ocean were not retrieved.



Given the latitude  $\varphi$ , we can calculate solar zenith angle  $\theta$  for GMT  $t$  used in the production from the following formula:

$$\theta(t) = \arccos[\sin \varphi \sin \delta + \cos \varphi \cos \delta \cos(\frac{t - 12}{12}180)], \quad (10)$$

where  $\delta$  is Earth declination angle, which can be calculated from day of year (DOY) as:

$$\delta = 23.45 \sin(360 \frac{283 + DOY}{365}). \quad (11)$$

## 2.7 Product description

The DSR and PAR products are available in two separate datasets: MCD18A1 (DSR) and MCD18A2 (PAR). MCD18A1 and MCD18A2 are gridded L3 products in MODIS sinusoidal map projection with 5km resolution. One product file is produced for one day over one MODIS sinusoidal land tile. Names of MCD18A1 and MCD18A2 follow the file naming convention of standard MODIS products.

MCD18A1 and MCD18A2 files are archived in Hierarchical Data Format V4 - Earth Observing System (HDF-EOS) format files. Each file contains global attributes (metadata) and scientific data sets (SDSs, data layers). Each file contains two major types of scientific data sets: instantaneous DSR/PAR array for each individual MODIS overpass and 3-hour DSR/PAR array. The 3-hour data are available at GMT 0:00, 3:00, 6:00, 9:00, 12:00, 15:00, 18:00, and 21:00. An example of global maps of 3-hourly DSR product is displayed in Figure 6. It shows the day times with large amounts of solar radiation moving from the east to the west.

## 3. Validation

### 3.1 Algorithm validation

The detailed results can be found in our earlier publications (Liang et al., 2006, 2007). The validation experiments were conducted using ground measurements of incident PAR at six FLUXNET sites (Fort Peck, Montana; Lost Creek, Wisconsin; Oak Ridge, Tennessee; Walker Branch, Tennessee; Santa Rem, Brazil; and Black Hills, South Dakota) from 2002-2004. For each site, a 3km \* 3km window (9 pixels) of the MODIS TOA radiance (MOD02) and angular values were extracted from the MODIS datasets ordered from the EOS Gateway. The ground measurements collected every half-hour or one hour were compared with the retrieved values. The measurement values closest to the time of MODIS data acquisition were used to compare with the value of the central pixel in the extracted 9-pixel window without any interpolation.

Figure 7 shows the validation results at six FLUXNET sites. The correlation coefficient between MODIS instantaneous PAR and ground-based measurements is 0.95. MODIS instantaneous PAR has a bias of  $32.5 \mu \text{ mol s}^{-1} \text{ m}^{-2}$  (2.9% in relative value), and an RMSE of  $194.8 \mu \text{ mol s}^{-1} \text{ m}^{-2}$

(17.5% in relative value). Our latest study demonstrated that aggregating MODIS products spatially and ground measurements temporally can produce much better results.

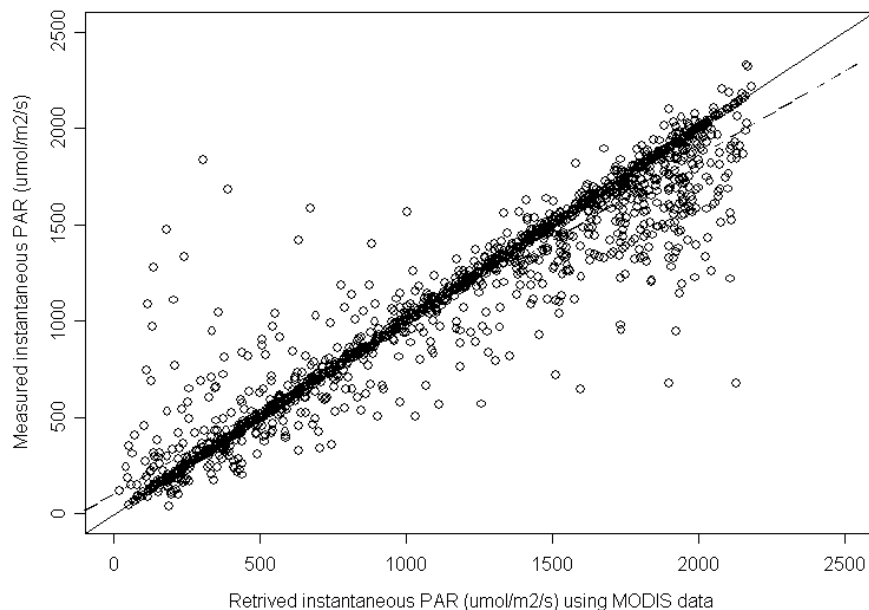


**Figure 7.** Validation of MODIS-derived instantaneous PAR data at six FLUXNET sites (Fort Peck, Montana; Lost Creek, Wisconsin; Oak Ridge, Tennessee; Walker Branch, Tennessee; Santa Rem, Brazil; and Black Hills, South Dakota) from 2002-2004. For each site, a 3km \* 3km window (9 pixels) of the MODIS TOA radiance (MOD02) and angular values were extracted from the MODIS datasets ordered from the EOS Gateway. The ground measurements collected every half-hour or one hour were compared with the retrieved values. The solid line is the 1:1 line, the dashed line is the best fit line based on least squares regression.

Additional validation results summarized in Table 3 demonstrate that the DSR and PAR retrievals are accurate under all sky conditions (Zhang et al. 2014). The overall coefficient of determination at these sites is 0.83 and 0.84 for DSR and PAR, respectively. The bias values for DSP and PAR are  $-6.5 \text{ Wm}^{-2}$  and  $5.0 \text{ Wm}^{-2}$ , respectively, and the RMSE values are  $115.0 \text{ Wm}^{-2}$  and  $49.0 \text{ Wm}^{-2}$ , respectively. As shown in Table 3, the validation results at the SURFRAD sites are better than those at other sites except the Desert Rock site, which may be due to the time scales released by the data centers. The SURFRAD sites released the measurements every 3 min and are always believed to have better quality; however, a 30 minute average was used for the CarbonEuropeIP and COIRAS sites. The validation results at the Desert Rock site show the maximum RMSE of  $55 \text{ Wm}^{-2}$ . To obtain more insight in to the discrepancies at Desert Rock, we further investigated the details of this site. The Desert Rock ( $36.63^\circ\text{N}$ ,  $116.02^\circ\text{W}$ ) site at SURFRAD, which is located 65 miles northwest of Las Vegas, has an elevation higher than 1000 m. Its land surface is covered by fine rock and scattered desert shrubs. We speculate that the systematic errors are primarily due to the climatic conditions, the

altitude, and the absolute accuracy of the pyrometer at this site. The absolute accuracy of pyrometers has never been better than 5% or  $10 \text{ Wm}^{-2}$ .

**Table 3.** A summary of the statistics of the comparison of the ground measurements and the estimated DSR and PAR at the 34 sites. The DSR and PAR results retrieved from MODIS data were compared with the 30 min average of the field measurements of DSR and PAR to reduce the possible mismatch of space and time at these selected sites. The accuracy was assessed by applying three widely used statistical estimators (coefficient of determination ( $R^2$ ), root mean square error (RMSE), and mean bias error (BIAS)). The unit for bias and RMSE is  $\text{W/m}^2$

Site	DSR			PAR		
	$R^2$	Bias	RMSE	$R^2$	Bias	RMSE
Bondville	0.86	20	100	0.86	4.6	45
FortPeck	0.82	5.5	111	0.82	1.6	46
Goodwin Creek	0.92	1.7	86	0.91	4.2	38
Penn State	0.87	12	100	0.86	9.4	44
Sioux Falls	0.86	14	102	0.86	2.4	43
Boulder	0.77	-8.7	140	0.78	-7.6	58
Desert Rock	0.88	-55	119	0.89	-30	51
ARM-SGP Main	0.9	-7.73	93	0.88	16	45
Audubon Research Ranch	0.86	-42	120	0.87	24	56
Brookings	0.83	-9	114	0.84	33	55
Fermi Agricultural	0.77	55	145	0.78	2	61
Flagstaff Managed Forest	0.78	-26	150	0.77	-19	68
Flagstaff UnManaged Forest	0.86	-24	110	0.88	-4	44
Neustift	0.8	-48	140	0.83	-5	48
Lonzee	0.6	2	131	0.74	9	48
Vielsalm	0.75	12	107	0.79	22	47
Laegeren	0.77	-41	146	0.83	-4	49
Oensingen2_crop	0.77	-10	129	0.86	-9	47
Bily Kriz-Beskidy Mountains	0.77	17	121	0.83	24	48
Bily Kriz grassland	0.79	-3	119	0.82	25	49
CZECHWET	0.88	-17	84	0.86	11	41
Moldova	0.89	34	97	0.85	7	47
Alta_Floresta	0.87	2	108			
CEILAP-BA	0.82	-23	123			
Kherlenbayan Ulaan	0.9	31	94			
Arou	0.83	-23	119			
Changwu	0.82	24	111			
Dayekou	0.84	-20	133			

Dingxi	0.85	16	101			
Dongsu	0.85	-44	115	0.82	-5	48
Tongyu	0.81	-8	106			
Yingke	0.85	-31	117			
Yuzhong	0.8	-22	131			
Zhangye	0.87	-6	93			
Total	0.83	-6.5	115	0.84	5	49

### 3.2 Product validation

With the availability of the data products operationally generated from MODAPS, we are able to assess the data quality of the actual products. Field measurements of DSR and PAR at the seven SURFRAD stations in 2004 were used in product validation.

The preliminary validation results suggest that the new MODIS DSR and PAR 3-hour products are reliable and highly accurate (Figure 8 and Table 4). DSR and PAR have the overall coefficients of determination of 0.91 and 0.92 respectively. MCD18A1 has a RMSE of 90  $W/m^2$ , bias of 17  $W/m^2$ . MCD18A2 has a RMSE of 39  $W/m^2$ , bias of 9  $W/m^2$ . The results by sites can be found in Table 4. All the seven SURFRAC sites show slight overestimation with positive biases ranging from 3.8-22  $W/m^2$  for DSR and -0.5-14  $W/m^2$  for PAR. RMSE of estimating DSR varies from the smallest value of 72  $W/m^2$  at Desert Rock to the largest error of 106  $W/m^2$  at Boulder. RMSE of estimating PAR varies from the smallest value of 28  $W/m^2$  at Desert Rock to the largest error of 44  $W/m^2$  at Bolder.

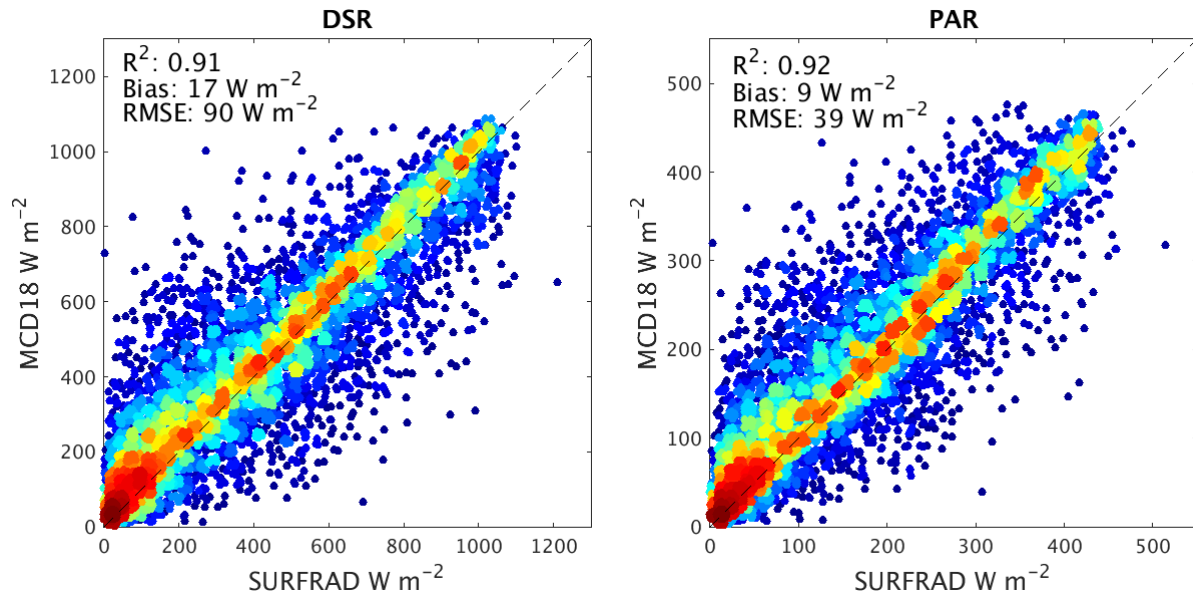


**Figure 8.** Validation results of MCD18A1 and MCD18A2 3-hour products using the field measurements of DSR and PAR collected at SURFRAD stations. The MODIS DSR and PAR products over all the seven SURFRAD stations during 2004 were used in comparison. Data averaged from the MODIS 4 by 4 pixels centered the SURFRAD stations were compared against with mean values of 1-minute field measurements during a time window of 30 minutes around the MODIS product time.

**Table 4.** Summary statistics of validating MCD18A1 and MCD18A2 3-hour products using the field measurements of DSR and PAR collected at SURFRAD stations. The MODIS DSR and PAR products over all the seven SURFRAD stations during 2004 were used in comparison. Data averaged from the MODIS 4 by 4 pixels centered the SURFRAD stations were compared against with mean values of 1-minute field measurements during a time window of 30 minutes around the MODIS product time. The unit for both bias and RMSE is W/m<sup>2</sup>.

Site	DSR (MCD18A1)			PAR (MCD18A2)		
	R <sup>2</sup>	Bias	RMSE	R <sup>2</sup>	Bias	RMSE
Bondville	0.89	21	95	0.90	13	43
FortPeck	0.92	22	82	0.93	9.3	33
Goodwin Creek	0.91	20	88	0.91	14	42
Penn State	0.89	16	91	0.90	12	40
Sioux Falls	0.90	23	92	0.92	10	38
Boulder	0.88	11	106	0.89	5.1	44
Desert Rock	0.96	3.8	72	0.97	-0.5	28

#### 4. Constraints, limitations, and assumptions

Data from multiple geostationary satellites were initially proposed to be used as the ancillary input to MODIS data to improve temporal coverage at low latitudes. However, the existing MODAPS system uses MODIS data as the main satellite input, and we had difficulty incorporating geostationary satellite data into the production. For operational purposes, we have modified our codes and deactivated the module of processing geostationary data. The current operational codes use only Terra and Aqua MODIS data as the main input satellite data. The geostationary modules can be activated in the future when geostationary satellite data are available through the MODAPS system.

The LUT based approach uses MODIS TOA reflectance data of the blue band as the main input. It does not require various atmospheric parameters and thus can avoid errors caused by unavailability and uncertainties of these parameters. However, such simplification also has its limitations under some circumstances. The limited spectral information used in the LUT approach may translate into substantial uncertainties in complex cloudy cases. We have developed alternative retrieval approaches based on parameterization and optimization schemes. We also have developed a framework of product integration. An integrated product that combines results from the LUT method, parameterization scheme and optimization approach can be used to address such issues.

#### 5. References

Baret, F., Hagolle, O., Geiger, B., Bicheron, P., Miras, B., Huc, M., Berthelot, B., Nino, F., Weiss, M., Samain, O., Roujean, J.L., & Leroy, M. (2007). LAI, fAPAR and fCover CYCLOPES global products derived from VEGETATION - Part 1: Principles of the algorithm. *Remote Sensing of Environment*, 110, 275-286

Cai, W.W., Yuan, W.P., Liang, S.L., Zhang, X.T., Dong, W.J., Xia, J.Z., Fu, Y., Chen, Y., Liu, D., & Zhang, Q. (2014). Improved estimations of gross primary production using satellite-derived photosynthetically active radiation. *Journal of Geophysical Research-Biogeosciences*, *119*, 110-123

Cramer, W., Churkina, G., Nemry, B., Ruimy, A., Schloss, A.L., Kicklighter, D.W., Bondeau, A., & Moore, I.B. (1999). Comparing global models of terrestrial Net Primary Productivity (NPP): Overview and key results. *Global Change Biology*, *5*, 1-15

Dubayah, R. (1992). Estimating net solar-radiation using Landsat Thematic Mapper and digital elevation data. *Water Resources Research*, *28*, 2469-2484

Gui, S., Liang, S., Wang, K., & Li, L. (2010). Assessment of Three Satellite-Estimated Land Surface Downward Shortwave Radiation Datasets *Ieee Geoscience and Remote Sensing Letters*, *7*, 776-780

Hicke, J.A. (2005). NCEP and GISS solar radiation data sets available for ecosystem modeling: Description, differences, and impacts on net primary production. *Global Biogeochemical Cycles*, *19*, GB2006, doi:2010.1029/2004GB002391

Kim, H.Y., & Liang, S. (2010). Development of a hybrid method for estimating land surface shortwave net radiation from MODIS data. *Remote Sensing of Environment*, *114*, 2393-2402

Liang, S. (2004). *Quantitative remote sensing of land surfaces*. Hoboken, New Jersey: John Wiley & Sons, Inc

Liang, S., Wang, K., Zhang, X., & Wild, M. (2010). Review on Estimation of Land Surface Radiation and Energy Budgets From Ground Measurement, Remote Sensing and Model Simulations. *IEEE Journal of Selected Topics in Applied Earth Observations and Remote Sensing*, *3*, 225-240

Liang, S., Zheng, T., Liu, R., Fang, H., Tsay, S.C., & Running, S. (2006). Estimation of incident photosynthetically active radiation from Moderate Resolution Imaging Spectrometer data. *Journal of Geophysical Research-Atmospheres*, *111*

Liang, S., Zheng, T., Wang, D., Wang, K., Liu, R., Tsay, S.C., Running, S., & Townshend, J. (2007). Mapping high-resolution incident photosynthetically active radiation over land from polar-orbiting and geostationary satellite data. *Photogrammetric Engineering and Remote Sensing*, *73*, 1085-1089

Liu, R., Liang, S., He, H., Liu, J., & Zheng, T. (2008). Mapping incident photosynthetically active radiation from MODIS data over China. *Remote Sensing of Environment*, *112*, 998-1009

- Lu, N., Liu, R.G., Liu, J.Y., & Liang, S. (2010). An algorithm for estimating downward shortwave radiation from GMS 5 visible imagery and its evaluation over China. *Journal of Geophysical Research-Atmospheres*, 115
- Myneni, R.B., Hoffman, S., Knyazikhin, Y., Privette, J.L., Glassy, J., Tian, Y., Wang, Y., Song, X., Zhang, Y., Smith, G.R., Lotsch, A., Friedl, M., Morisette, J.T., Votava, P., Nemani, R.R., & Running, S.W. (2002). Global products of vegetation leaf area and fraction absorbed PAR from year one of MODIS data. *Remote Sensing of Environment*, 83, 214-231
- Nemani, R., Keeling, C., Hashimoto, H., Jolly, W., Piper, S., Tucker, C., Myneni, R., & Running, S. (2003). Climate-driven increases in global terrestrial net primary production from 1982 to 1999. *Science*, 330, 1560-1563
- Potter, C.S., Randerson, J.T., Field, C.B., & Matson, P.A. (1993). Terrestrial ecosystem production: A process model based on global satellite and surface data. *Global Biogeochemical Cycles*, 7, 811-841
- Prince, S.D., & Goward, S.N. (1995). Global primary production: A remote sensing approach. *Journal of Biogeography*, 22, 815-835
- Psiloglou, B.E., Santamouris, M., & Asimakopoulos, D.N. (2000). Atmospheric broadband model for computation of solar radiation at the earth's surface. Application to Mediterranean climate. *Pure and Applied Geophysics*, 157, 829-860
- Sellers, P.J., Mintz, Y., Sud, Y.C., & Dalcher, A. (1986). A simple biosphere model (SiB) for use within general circulation models. *Journal of the Atmospheric Sciences*, 43, 505-531
- Tang, H., Yu, K., Hagolle, O., Jiang, K., Geng, X., & Zhao, Y. (2013). A cloud detection method based on a time series of MODIS surface reflectance images. *International Journal of Digital Earth*, 6, 157-171
- Trenberth, K.E., Fasullo, J.T., & Kiehl, J. (2009). Earth's Global Energy Budget. *Bulletin of the American Meteorological Society*, 90, 311-323
- Wang, D., Liang, S., Liu, R., & Zheng, T. (2010). Estimation of daily-integrated PAR from sparse satellite observations: comparison of temporal scaling methods. *International Journal of Remote Sensing*, 31, 1661-1677
- Wang, K., & Dickinson, R.E. (2012). A Review of Global Terrestrial Evapotranspiration: Observation, Modeling, Climatology, and Climatic Variability. *Reviews of Geophysics*, 50, RG2005, doi:2010.1029/2011RG000373

Wild, M. (2012). Enlightening global dimming and brightening. *Bulletin of the American Meteorological Society*, 93, 27-37

Xiao, Z.Q., Liang, S., Sun, R., Wang, J.D., & Jiang, B. (2015). Estimating the fraction of absorbed photosynthetically active radiation from the MODIS data based GLASS leaf area index product. *Remote Sensing of Environment*, 171, 105-117

Zhang, X., Liang, S., Wang, G., Yao, Y., Jiang, B., & Cheng, J. (2016). Evaluation of the Reanalysis Surface Incident Shortwave Radiation Products from NCEP, ECMWF, GSFC, and JMA Using Satellite and Surface Observations. *Remote Sensing*, 8

Zhang, X., Liang, S., Wild, M., & Jiang, B. (2015). Analysis of surface incident shortwave radiation from four satellite products. *Remote Sensing of Environment*, 165, 186-202

Zhang, X., Liang, S., Zhou, G., Wu, H., & Zhao, X. (2014). Generating Global LAnd Surface Satellite incident shortwave radiation and photosynthetically active radiation products from multiple satellite data. *Remote Sensing of Environment*, 152, 318-332

Zhao, M., Running, S., & Nemani, R. (2006). Sensitivity of Moderate Resolution Imaging Spectroradiometer (MODIS) terrestrial primary production to the accuracy of meteorological reanalyses. *Journal of Geophysical Research*, 111, G01002, doi:01010.01029/02004JG000004

Zheng, T., Liang, S., & Wang, K. (2008). Estimation of incident photosynthetically active radiation from GOES visible imagery. *Journal of Applied Meteorology and Climatology*, 47, 853-868